Modeling Dual Active Bridge Converters in DC Distribution Systems

Jacob A. Mueller, *Member, IEEE*, and Jonathan W. Kimball, *Senior Member, IEEE*

***Abstract*—Modeling improvements are proposed for systems containing dual active bridge (DAB) converters. First, a systematic approach to constructing models of multiconverter systems is described. The method generates continuous-time large-signal average models that are suitable for system-level analysis and efficient time-domain simulation. Although the base DAB models are derived using generalized average modeling (GAM), the system-level construction does not require the specification of a base period. Second, a method of reconstructing currents in the high-frequency DAB transformer is proposed. This method significantly improves accuracy in modeling transformer current, which is a critical weakness of DAB models derived using GAM. Furthermore, the method is applied offline as needed, so it does not affect the computational complexity of time-domain simulation. Both the system-level model construction procedure and harmonic reconstruction method are validated in switching simulations and hardware experiments.**

***Index Terms*—Average modeling, dual active bridge (DAB) converter, generalized average model, phase shift modulation.**

I. Introduction

DUAL active bridge (DAB) converters are well-suited to applications in power distribution systems due to their high power density, low device stresses, galvanic isolation, and bidirectional operation [1]–[3]. DAB converters have been considered as a candidate topology for solid-state transformers [4], [5] and have been studied in the context of automotive [6], aerospace [7], and marine power systems [8], [9]. In all of these applications, the ability to accurately describe the behavior of the DAB converter—and its interactions with other converters in the system—is of critical importance. System-level analyses, such as stability assessments and time-domain simulation, depend on models that are both accurate and scalable. This study is concerned with the development of models that meet these criteria.

Modeling DAB converters are difficult due to the presence of a high-frequency ac conversion stage and ac state variables. The most popular strategy for dealing with this challenge is to employ the sampled-data modeling method from [10]. This method produces discrete-time models that provide exact state

Manuscript received January 29, 2018; revised April 27, 2018 and July 13, 2018; accepted August 17, 2018. Date of publication August 27, 2018; date of current version April 20, 2019. This work was supported by the National Science Foundation under award 1406156. Recommended for publication by Associate Editor D. Xu. *(Corresponding author: Jacob A. Mueller.)*

The authors are with the Department of Electrical and Computer Engineering, Missouri University of Science and Technology, Rolla, MO 65409 USA (e-mail:

accuracy, the model derived using GAM is less suitable for efficient time-domain simulation due to high computational complexity. However, in the case of a DAB converter, it is possible to mitigate scalability issues using structural properties of the model. In particular, the state equations of the original model in [17] are decoupled along lines of physical relevance, making it possible to consider only the states of interest in the final model. The same decoupling effect exists for systems of multiple DAB converters as well [21].

The specific system-level analysis tasks of interest in this study are time-domain simulation and small-signal stability assessment. Time-domain simulation is an important analysis tool for all power distribution systems. For conventional (ac) power systems, time-simulations involve numerical integration of a nonlinear large-signal model [22], [23]. Simulation of power electronic systems is more complex due to the inherent discontinuities of switched-mode converters. The most accurate simulations involve switched models, wherein the active switch configuration determines the model used in the integration routine [24]–[26]. However, discontinuities at switch transitions cause complications for numerical integration algorithms, ranging from difficulties in step size selection to numerical convergence issues [27]. As a result, switching simulations are slow, and scale poorly with the number of switched-mode devices in a given system [28], [29]. To address this issue, the average modeling approach (both in the classical low-frequency and generalized sense) consolidates models associated with each switch configuration into a single representation [16], [30]–[32]. The averaging process eliminates switching discontinuities and improves the efficiency of numerical simulations [28], [29], [33]. However, averaging introduces an approximation, which may affect the accuracy of the final model [28], [34]. Average models of DAB converters are affected by errors due to averaging [14], [17], most notably in the transformer current state. To produce accurate and efficient system-level models, these errors must be eliminated without increasing model complexity.

Small-signal stability assessment is another essential analysis task. In power electronic systems, small-signal stability is most commonly assessed through impedance criteria (for a comprehensive review of impedance criteria, see [35] and references therein). The advantage of impedance criteria methods is that they do not require a system-level dynamic model to apply. However, the applicable criterion for a given system depends on the network topology and power flow configuration, and becomes difficult to apply for large systems, particularly when bidirectional converters are present. In power system analysis, small-signal stability is assessed by linearizing a system model and inspecting eigenvalues [23], [36]. This is a more flexible and scalable approach, but it requires a system-level model.

This study presents two contributions. The first is a method of constructing accurate and scalable models of systems containing multiple DAB converters. Models generated using this method are suitable for fast time-domain simulation or linearization for small-signal stability analysis. The method is presented in the context of a dc distribution system that contains only DAB converters, though the modeling approach itself does not preclude other converter topologies. The second contribution is a procedure for reconstructing exact transformer currents (and the currents in other converter elements) from the simplified first harmonic representation. The reconstruction process is applied offline, so it improves the fidelity of time-domain state solutions without affecting computational complexity. Both the contributions support the development of accurate and efficient representations of DAB converters in multiconverter systems.

The structure of the paper is as follows. Section II describes the large-signal DAB model, which is used as a modular element of the system-level model. Section III discusses the model construction procedure. The method of reconstructing transformer currents is proposed in Section IV. Verification experiments are discussed in Section V.

II. Base DAB Converter Model

A. GAM Framework

The GAM approach begins with the Fourier series representation of a state variable. For generic state variable $z(t)$, the Fourier series representation is

$$z(t) = \sum_{k=-\infty}^{\infty} \langle z \rangle_k(t) e^{j\omega k t} \tag{1}$$

where f_s is the converter switching frequency and $\omega = 2\pi f_s$. The angle-bracket term $\langle z \rangle_k(t)$ is the kth harmonic coefficient, and is defined by a sliding average over the switching period, T

$$\langle z \rangle_k(t) = \frac{1}{T} \int_{t-T}^{t} z(\tau) e^{-j\omega k \tau} d\tau. \tag{2}$$

These are the generalized averaging operations that define GAM. Classical state-space averaging may be viewed as a special case of the GAM framework, in which only $k = 0$ terms are considered. The dc average component $\langle z \rangle_0(t)$ is equivalent to the representation of $z(t)$ in a model derived using classical state-space averaging.

Two additional relationships are used in the application of GAM [16], [37]. The derivative of the harmonic coefficients is given by

$$\frac{d}{dt}\langle z \rangle_k(t) = \left\langle \frac{d}{dt} z \right\rangle_k (t) - j\omega k \langle z \rangle_k(t). \tag{3}$$

The product of coefficients is

$$\langle z \cdot y \rangle_k(t) = \sum_{i=-\infty}^{\infty} \langle z \rangle_{k-i}(t) \cdot \langle y \rangle_i(t). \tag{4}$$

Under a first harmonic approximation, ($k = 0, \pm 1$) the time-domain state may be recovered from the harmonic components as

$$\begin{aligned} z(t) &= \langle z \rangle_1(t) e^{j\omega t} + \langle z \rangle_{-1}(t) e^{-j\omega t} + \langle z \rangle_0(t) \\ &= 2\big(\langle z \rangle_R(t) \cos \omega t - \langle z \rangle_I(t) \sin \omega t\big) + \langle z \rangle_0(t) \end{aligned} \tag{5}$$

where $\langle z \rangle_R(t) = \Re[\langle z \rangle_1(t)]$ and $\langle z \rangle_I(t) = \Im[\langle z \rangle_1(t)]$ are the real and imaginary components of the first harmonic coefficient. This approximation limits both the complexity and large-signal accuracy of the final model, since higher-order terms are neglected. However, in the case of a DAB converter, the large-signal error may be corrected through the use of an algebraic correction factor [18].

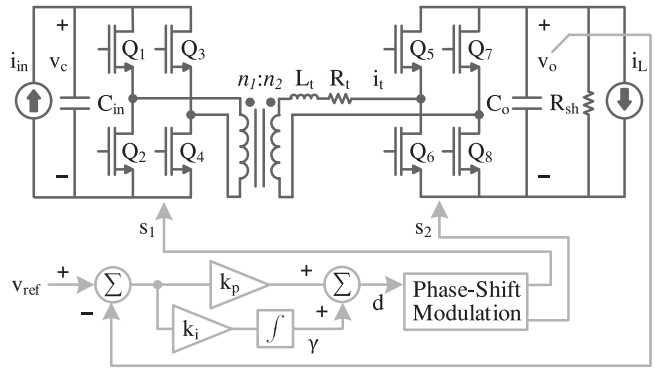

Fig. 1. Voltage-controlled DAB converter and control system.

B. Single Converter Model

This study uses the improved DAB model from [18] as a fundamental building block for the construction of a system level model. This model is referred to here as the "base" model, since it provides the basis for the system-level model construction procedure. The model in [18] is based on [17], but includes a correction factor to eliminate large-signal errors introduced by the first harmonic approximation. The correction equation does not change the model state equations, so the original formulation in [17] is relevant to the present discussion. Since the objective is to analyze the converter behavior in a full system, the closed-loop formulation is used. A diagram of the converter and control system is shown in Fig. 1. To simplify notation, transformers are assumed to have a 1:1 turns ratio throughout.

Before applying the GAM framework, the state equations are as follows:

$$\dot{v}_c = \frac{1}{C_{\text{in}}} i_{\text{in}} - \frac{1}{C_{\text{in}}} s_1 i_t \tag{6}$$

$$\dot{v}_o = \frac{-1}{R_{\text{sh}} C_o} v_o + \frac{1}{C_o} i_t s_2 - \frac{1}{C_o} i_L \tag{7}$$

$$\dot{i}_t = \frac{1}{L_t} v_c s_1 - \frac{1}{L_t} v_o s_2 - \frac{R_t}{L_t} i_t. \tag{8}$$

In these equations, dot notation denotes time derivatives, v_c is the input capacitor voltage, v_o is the output capacitor voltage, i_t is transformer current, and i_{in} is input current. When a voltage source is used instead of a current source, v_c is simply replaced by an input voltage v_{in}, and (6) is eliminated. Current source i_L and shunt resistance R_{sh} define a Norton equivalent load. Capacitances of the input and output bus capacitors are C_{in} and C_o, respectively. Transformer leakage inductance is L_t, and parasitic winding resistance is R_t. Switching functions s_1 and s_2 are as follows:

$$s_1 = \begin{cases} 1, & 0 \le \tau < \frac{T}{2} \\ -1, & \frac{T}{2} \le \tau < T \end{cases} \tag{9}$$

$$s_2 = \begin{cases} 1, & \frac{dT}{2} \le \tau < \frac{dT}{2} + \frac{T}{2} \\ -1, & 0 \le \tau < \frac{dT}{2} \quad \text{or} \quad \frac{dT}{2} + \frac{T}{2} \le \tau < T \end{cases} \tag{10}$$

where T is the length of a single switching period, τ is the time within the switching period, and d is the converter phase shift. This study follows the phase shift terminology of [3], [14], [17]; i.e., $d = \frac{\phi}{\pi}$, where ϕ is the phase shift in radians. All of these hardware and control parameters are identified in Fig. 1.

Next, the GAM framework is applied. In the following equations, angle brackets for GAM states are dropped in the interest of readability, and states are identified using subscripts. For example, the dc average of generic state z is denoted z_0; real and imaginary components of the first harmonic component are denoted by z_R and z_I, respectively. This notation is used for the remainder of the paper.

The state and input vectors of the model are as follows:

$$x = [v_{c0} \quad v_{o0} \quad i_{tR} \quad i_{tI} \quad \gamma_0]^T \tag{11}$$

$$u = [i_{\text{in}0} \quad i_{L0} \quad v_{\text{ref}}]^T. \tag{12}$$

The GAM state equations are as follows:

$$\dot{v}_{c0} = \frac{1}{C_{\text{in}}} i_{\text{in}0} + \frac{4}{C_{\text{in}}\pi} i_{tI} \tag{13}$$

$$\dot{v}_{o0} = \frac{-1}{R_{\text{sh}} C_o} v_{o0} - \frac{4 \sin \pi \hat{d}}{C_o \pi} i_{tR} - \frac{4 \cos \pi \hat{d}}{C_o \pi} i_{tI} - \frac{1}{C_o} i_{L0} \tag{14}$$

$$\dot{i}_{tR} = \frac{2 \sin \pi \hat{d}}{L_t \pi} v_{o0} - \frac{R_t}{L_t} i_{tR} + \omega i_{tI} \tag{15}$$

$$\dot{i}_{tI} = \frac{2 \cos \pi \hat{d}}{L_t \pi} v_{o0} - \omega i_{tR} - \frac{R_t}{L_t} i_{tI} - \frac{2}{L_t \pi} v_{c0} \tag{16}$$

$$\dot{\gamma_0} = k_i \left(v_{\text{ref}} - v_{o0} \right) \tag{17}$$

where ω is the switching frequency in radians per second and k_i is the integral gain of the voltage controller. Again, in the case of a voltage source, v_{c0} is replaced by $v_{\text{in}0}$ in (16), $i_{\text{in}0}$ is replaced by $v_{\text{in}0}$ in (12), and state equation (13) becomes unnecessary.

Note that the phase shift arguments in (13)–(17) appear as $\hat{d}$, whereas phase shift appears as d in (9), (10), and Fig. 1. This difference is intentional: for a given input voltage/current and load, the phase shift value that satisfies the equilibrium solution of the model equations ($\hat{d}$) is not the same as the corresponding phase shift observed in switching simulations or hardware experiments (d). If the two are assumed to be equal, the state equations above will be affected by persistent steady-state error, and the large-signal model will be inaccurate [14], [38].

A correction factor was proposed in [18] as an algebraic function of the two phase shift variables. The actual phase shift d is the output of the voltage controller

$$d = k_p (v_{\text{ref}} - v_{o0}) + \gamma_0 \tag{18}$$

where k_p is proportional gain. The model equilibrium phase shift, $\hat{d}$, is represented internally as an algebraic state. The relationship between $\hat{d}$ and the rest of the model is described by the following:

$$\begin{aligned} 0 = g(x, \hat{d}, u) = & -v_{c0} R_t \cos \pi \hat{d} - v_{c0} X_t \sin \pi \hat{d} \\ & + v_{o0} R_t + K \left(v_{c0} - v_{o0} \right) \theta + K v_{o0} \tanh \theta \\ & + K v_{c0} \frac{d}{|d|} \left(1 - 2\theta d - \operatorname{sech} \theta \exp \left(\frac{d}{|d|} \theta - 2\theta d \right) \right) \end{aligned} \tag{19}$$

where $X_t = \omega L_t$ is transformer reactance and K and θ are the following hardware constants:

$$K = \frac{\pi}{4}\frac{X_t(R_t^2 + X_t^2)}{R_t^2} \tag{20}$$

$$\theta = \frac{\pi R_t}{2X_t}. \tag{21}$$

The full large-signal model is a system of differential algebraic equations with the form

$$\dot{x} = f(x, \hat{d}, u) \tag{22}$$

$$0 = g(x, \hat{d}, u) \tag{23}$$

where $f(\cdot)$ contains (13)–(17) and $g(\cdot)$ is defined in (19).

C. Decoupling Effect and Selective Averaging

Under the first harmonic approximation, each variable z is broken into three components corresponding to the $k = 0, \pm 1$ averages or, equivalently, z_0, z_R, and z_I. However, only a subset of these appear in the state and input vectors (11). Namely, the dc states (capacitor voltages and integrator) are represented only be dc average ($k = 0$) terms, while the ac transformer currents are represented by the $k = \pm 1$ terms. This is because the remaining terms are decoupled from states the in (11) [17]. Furthermore, the influence of ac inputs (namely i_{inR}, i_{inI}, i_{oR}, and i_{oI}) is entirely confined to the decoupled states.

In previous studies, the number of Fourier series terms used to represent each state variable was selected according to the dominant dynamics of that state [19]. This is referred to as "selective averaging," and it assumes some *a priori* knowledge of system dynamics. If this process were applied to the DAB model, only the transformer current would be modeled by $k = \pm 1$ terms, since it is the only ac state. Conveniently, the structural properties of the DAB model provide this exact result without the use of assumptions to selectively eliminate undesirable terms.

The real importance of the decoupling effect is that the terminal characteristics of each converter may be represented by dc average terms only without sacrificing model validity. This has significant implications for the system-level model. Interactions between each converter and the rest of the system may be described using dc average states and equations. The $k = \pm 1$ components of these interactions, which are frequency dependent, may be safely ignored. More precisely, when included in the derivation of the system-level model, the $k = \pm 1$ components of terminal voltages and line currents are contained in a subsystem that is decoupled from the dc average line currents and the states in (11). This was shown in [21], an earlier version of this study. Modeling the frequency dependent interactions of this subsystem would require the specification of a system-wide base period, and would undercut the scalability and modularity objectives of the model construction process. Since it is possible to neglect these interactions from the model with no ill effect, the methods shown here focus on dc average interactions and states in (11). The following section describes a procedure that operates directly on the models in (22). The method results in the same final model as the derivation shown in [21], but is simpler and more concise.

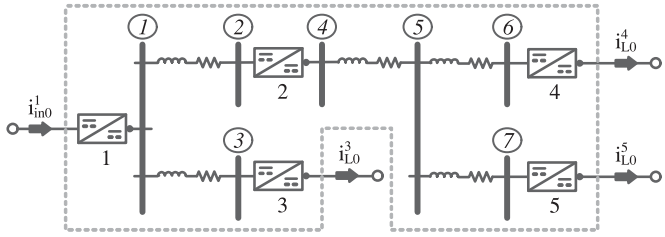

Fig. 2. Five-converter example system. Each converter is shown a two-port element, with the (controlled) output port denoted by a dot. Encircled integers are system bus numbers. The dotted line indicates the scope of the system-level model.

III. System-Level Model

The model construction procedure described in this section uses the large-signal converter model as a modular building block. The system under consideration consists of N converters and M buses. An example system with $N = 5$ and $M = 7$ is shown in Fig. 2 for the purpose of converter and bus numbering schemes. All converters are bidirectional and may connect to the system through the controlled output terminal, uncontrolled input terminal, or both. Superscripts are used to identify states, inputs, and parameters pertaining to each converter, e.g., x^n refers to the state vector of converter n.

A. Model Combination

The system has M buses, where $M \geq N$. Each bus may correspond to a converter input or output terminal or to a structural node with no converter present (e.g., bus 5 in Fig. 2). The lines in the system may be resistive or resistive/inductive. The latter is described, since it is more general. The line current between buses i and j is described by

$$i^{ij}_{\ell 0} = \frac{1}{L_{ij}}(v^i_{b0} - v^j_{b0}) - \frac{R_{ij}}{L_{ij}} i^{ij}_{\ell 0} \tag{24}$$

where v^i_{b0} and v^j_{b0} are the dc average voltages at buses i and j, R_{ij} and L_{ij} are the resistance and inductance of the line, and $i < j$ by convention.

To construct the system-level model, the points of interaction between the converters and the rest of the system must be expressed in terms of state variables. Specifically, the system-level model must incorporate self-contained descriptions of the output currents for all converters connected by output terminal, input currents of all converters connected by input terminal, and all bus voltages. This is done on a bus-by-bus basis. When bus m corresponds to the output terminal of converter n, the converter output current is

$$i^n_{L0} = -\sum_{i=1}^{m-1} i^{mi}_{\ell 0} + \sum_{j=m+1}^{M} i^{mj}_{\ell 0}. \tag{25}$$

This follows from the application of Kirchoff's current law (KCL) at bus m. Trivially, the bus voltage is equal to the con-

verter output voltage, i.e., $v_{b0}^m = v_{o0}^n$. Similarly, when bus m corresponds to the input terminal of converter n, the converter input current is

$$i_{in0}^n = \sum_{i=1}^{m-1} i_{\ell 0}^{mi} - \sum_{j=m+1}^{M} i_{\ell 0}^{mj}. \tag{26}$$

In this case, the bus voltage is equal to the input capacitor voltage ($v_{b0}^m = v_{c0}^n$).

In the final case, bus m is not connected to a converter. Bus 5 in Fig. 2 is an example of this case. By KCL, the current at this node is

$$0 = \sum_{i=1}^{m-1} i_{\ell 0}^{mi} - \sum_{j=m+1}^{M} i_{\ell 0}^{mj}. \tag{27}$$

Even though no converter is present, it is still necessary to represent the bus voltages in the model, since they are used in the line current equations. These bus voltages are included as algebraic state variables. For each bus m with no converter, the model contains both the voltage at the bus and the corresponding node current expression.

B. System-Level Organization

The full system-level model has the form

$$\dot{x}_{\text{sys}} = f_{\text{sys}}(x_{\text{sys}}, y_{\text{sys}}, u_{\text{sys}}) \tag{28}$$

$$0 = g_{\text{sys}}(x_{\text{sys}}, y_{\text{sys}}, u_{\text{sys}}). \tag{29}$$

The state vector x_{sys} is

$$x_{\text{sys}} = [x^1 \quad x^2 \quad \cdots \quad x^N \quad x_{\text{line}}]^T \tag{30}$$

where each x^n is a converter state vector and x_{line} is a vector containing all line current states. The algebraic state vector y_{sys} contains all internal phase shift variables and all bus voltages that are not already states in x_{sys}. The vector is

$$y_{\text{sys}} = [\hat{d}^1 \quad \hat{d}^2 \quad \cdots \quad \hat{d}^N \quad y_{\text{bus}}]^T \tag{31}$$

where y_{bus} contains the voltage v_{b0}^m of each bus m that does not correspond to the output terminal of a source converter or input terminal of a load converter.

The system-level input vector u_{sys} contains all N control inputs and all current inputs that are external to the system, i.e., all i_{in0}^n and i_{L0}^n not described by (25) and (26). The number of external connections depends on the topology of the system. For example, the input vector for the system shown in Fig. 2 is

$$u_{\text{sys}} = [i_{\text{in0}}^1 \;\; v_{\text{ref}}^1 \;\; v_{\text{ref}}^2 \;\; i_{L0}^3 \;\; v_{\text{ref}}^3 \;\; i_{L0}^4 \;\; v_{\text{ref}}^4 \;\; i_{L0}^5 \;\; v_{\text{ref}}^5]^T. \tag{32}$$

The four current terms in this vector correspond to the four external connections shown in Fig. 2.

The system equations $f_{\text{sys}}(\cdot)$ are (13)–(17) for each converter and (24) for each line current. Likewise, the equations in $g_{\text{sys}}(\cdot)$ are (19) for each converter and (27) for each voltage in y_{bus}.

To use the system-level model, partial derivative matrices are needed. For convenience, define function $\dot{x}_{\text{line}} = f_{\text{line}}(\cdot)$ to include all line current state equations and $0 = g_{\text{line}}(\cdot)$ to include all algebraic KCL equations for buses not connected to converters. The partial derivative matrices may then be described in terms of block submatrices

$$\frac{\partial f_{\text{sys}}}{\partial x_{\text{sys}}} = \begin{bmatrix} \frac{\partial f^1}{\partial x^1} & \cdots & 0 & \frac{\partial f^1}{\partial x_{\text{line}}} \\ \vdots & \ddots & \vdots & \vdots \\ 0 & \cdots & \frac{\partial f^N}{\partial x^N} & \frac{\partial f^N}{\partial x_{\text{line}}} \\ \frac{\partial f_{\text{line}}}{\partial x^1} & \cdots & \frac{\partial f_{\text{line}}}{\partial x^N} & \frac{\partial f_{\text{line}}}{\partial x_{\text{line}}} \end{bmatrix} \tag{33}$$

$$\frac{\partial f_{\text{sys}}}{\partial y_{\text{sys}}} = \begin{bmatrix} \frac{\partial f^1}{\partial \hat{d}^1} & \cdots & 0 & 0 \\ \vdots & \ddots & \vdots & \vdots \\ 0 & \cdots & \frac{\partial f^N}{\partial \hat{d}^N} & 0 \\ 0 & \cdots & 0 & \frac{\partial f_{\text{line}}}{\partial y_{\text{bus}}} \end{bmatrix} \tag{34}$$

$$\frac{\partial g_{\text{sys}}}{\partial x_{\text{sys}}} = \begin{bmatrix} \frac{\partial g^1}{\partial x^1} & \cdots & 0 & 0 \\ \vdots & \ddots & \vdots & \vdots \\ 0 & \cdots & \frac{\partial g^N}{\partial x^N} & 0 \\ 0 & \cdots & 0 & \frac{\partial g_{\text{line}}}{\partial x_{\text{line}}} \end{bmatrix} \tag{35}$$

$$\frac{\partial g_{\text{sys}}}{\partial y_{\text{sys}}} = \begin{bmatrix} \frac{\partial g^1}{\partial \hat{d}^1} & \cdots & 0 & 0 \\ \vdots & \ddots & \vdots & \vdots \\ 0 & \cdots & \frac{\partial g^N}{\partial \hat{d}^N} & 0 \\ 0 & \cdots & 0 & 0 \end{bmatrix}. \tag{36}$$

Each $\frac{\partial f^n}{\partial x^n}$ submatrix is the state matrix of converter n

$$\frac{\partial f^n}{\partial x^n} = \begin{bmatrix} 0 & 0 & 0 & \frac{4}{\pi C_{in}^n} & 0 \\ 0 & \frac{-1}{R_{sh}^n C_o^n} & \frac{-4\sin\pi\hat{d}^n}{\pi C_o^n} & \frac{-4\cos\pi\hat{d}^n}{\pi C_o^n} & 0 \\ 0 & \frac{2\sin\pi\hat{d}^n}{\pi L_t^n} & \frac{-R_t^n}{L_t^n} & \omega^n & 0 \\ \frac{-2}{\pi L_t^n} & \frac{2\cos\pi\hat{d}^n}{\pi L_t^n} & -\omega^n & \frac{-R_t^n}{L_t^n} & 0 \\ 0 & -k_i^n & 0 & 0 & 0 \end{bmatrix}. \tag{37}$$

The columns of $\frac{\partial f^n}{\partial x_{\text{line}}}$ and rows of $\frac{\partial f_{\text{line}}}{\partial x^n}$ are

$$\frac{\partial f^n}{\partial i_{\ell 0}^{ij}} = \begin{bmatrix} \frac{\partial(\dot{v}_{c0}^n)}{\partial i_{\ell 0}^{ij}} & \frac{\partial(\dot{v}_{o0}^n)}{\partial i_{\ell 0}^{ij}} & 0 & 0 & 0 \end{bmatrix}^T \tag{38}$$

$$\frac{\partial(\dot{i}_{\ell 0}^{ij})}{\partial x^n} = \begin{bmatrix} \frac{\partial(\dot{i}_{\ell 0}^{ij})}{\partial v_{c0}^n} & \frac{\partial(\dot{i}_{\ell 0}^{ij})}{\partial v_{o0}^n} & 0 & 0 & 0 \end{bmatrix}. \tag{39}$$

The elements of these vectors depend on how converter n connects to the system. For generality, let the input and output terminals of converter n correspond to buses p and q, respectively. Then, $v_{b0}^p = v_{c0}^n$ and $v_{b0}^q = v_{o0}^n$, and the partial derivative elements are as follows:

$$\frac{\partial(\dot{v}_{c0}^n)}{\partial i_{\ell 0}^{ij}} = \begin{cases} \frac{-1}{C_{in}^n}, & p = i \\ \frac{1}{C_{in}^n}, & p = j \\ 0, & \text{else} \end{cases} \qquad \frac{\partial(\dot{v}_{o0}^n)}{\partial i_{\ell 0}^{ij}} = \begin{cases} \frac{1}{C_o^n}, & q = i \\ \frac{-1}{C_o^n}, & q = j \\ 0, & \text{else} \end{cases}$$

$$\frac{\partial(\dot{i}_{\ell 0}^{ij})}{\partial v_{c0}^n} = \begin{cases} \frac{1}{L_{ij}}, & i = p \\ \frac{-1}{L_{ij}}, & j = p \\ 0, & \text{else} \end{cases} \qquad \frac{\partial(\dot{i}_{\ell 0}^{ij})}{\partial v_{o0}^n} = \begin{cases} \frac{1}{L_{ij}}, & i = q \\ \frac{-1}{L_{ij}}, & j = q \\ 0, & \text{else.} \end{cases}$$

Finally, submatrix $\frac{\partial f_{\text{line}}}{\partial x_{\text{line}}}$ is diagonal with elements

$$\frac{\partial(\dot{i}_{\ell 0}^{ij})}{\partial i_{\ell 0}^{ij}} = -\frac{R_{ij}}{L_{ij}}. \tag{40}$$

The nonzero submatrices of $\frac{\partial f_{\text{sys}}}{\partial y_{\text{sys}}}$ are $\frac{\partial f^n}{\partial \hat{d}^n}$ and $\frac{\partial f_{\text{line}}}{\partial y_{\text{bus}}}$. Each $\frac{\partial f^n}{\partial \hat{d}^n}$ is a column

$$\frac{\partial f^n}{\partial \hat{d}^n} = \begin{bmatrix} 0 \\ \frac{4}{C_o^n}\left(i_{tI}^n \sin\pi\hat{d}^n - i_{tR}^n \cos\pi\hat{d}^n\right) \\ \frac{2v_{o0}^n \cos\pi\hat{d}^n}{L_t^n} \\ \frac{-2v_{o0}^n \sin\pi\hat{d}^n}{L_t^n} \end{bmatrix}. \tag{41}$$

Submatrix $\frac{\partial f_{\text{line}}}{\partial y_{\text{bus}}}$ consists of elements $\frac{\partial(\dot{i}_{\ell 0}^{ij})}{\partial v_{b0}^m}$ for each line current $i_{\ell 0}^{ij} \in x_{\text{line}}$ and bus voltage $v_{b0}^m \in y_{\text{bus}}$. These elements are as follows:

$$\frac{\partial(\dot{i}_{\ell 0}^{ij})}{\partial v_{b0}^m} = \begin{cases} \frac{1}{L_{ij}}, & i = m \\ \frac{-1}{L_{ij}}, & j = m \\ 0, & \text{else.} \end{cases} \tag{42}$$

Matrix $\frac{\partial g_{\text{sys}}}{\partial x_{\text{sys}}}$ is a block diagonal combination of submatrices $\frac{\partial g^n}{\partial x^n}$ and $\frac{\partial g_{\text{line}}^m}{\partial x_{\text{line}}}$. The former is

$$\frac{\partial g^n}{\partial x^n} = \begin{bmatrix} \frac{\partial g^n}{\partial v_{c0}^n} & R_t^n - K^n\left(\theta^n - \tanh\theta^n\right) & 0 & 0 & \frac{\partial g^n}{\partial d^n} \end{bmatrix} \tag{43}$$

where $\frac{\partial g^n}{\partial v_{c0}^n}$ and $\frac{\partial g^n}{\partial d^n}$ are

$$\frac{\partial g^n}{\partial v_{c0}^n} = K^n\theta^n - R_t^n \cos\pi\hat{d}^n - X_t^n \sin\pi\hat{d}^n + K^n \frac{d^n}{|d^n|}\left(1 - 2\theta^n d^n - \operatorname{sech}\theta^n \exp\left(\frac{d^n}{|d^n|}\theta^n - 2\theta^n d^n\right)\right) \tag{44}$$

$$\frac{\partial g^n}{\partial d^n} = \frac{2d^n\theta K^n v_{c0}^n}{|d^n|}\left(\operatorname{sech}\theta^n \exp\left(\frac{d^n}{|d^n|}\theta^n - 2\theta^n d^n\right) - 1\right). \tag{45}$$

Submatrix $\frac{\partial g_{\text{line}}^m}{\partial x_{\text{line}}}$ has elements $\frac{\partial g_{\text{line}}^m}{\partial i_{\ell 0}^{ij}}$, where $g_{\text{line}}^m(\cdot)$ denotes the KCL equation applied at bus m. These elements are as follows:

$$\frac{\partial g_{\text{line}}^m}{\partial i_{\ell 0}^{ij}} = \begin{cases} 1, & m = i \\ -1, & m = j \\ 0, & \text{else.} \end{cases} \tag{46}$$

The last matrix $\frac{\partial g_{\text{sys}}}{\partial y_{\text{sys}}}$ has only diagonal elements $\frac{\partial g^n}{\partial \hat{d}^n}$, which are

$$\frac{\partial g^n}{\partial \hat{d}^n} = \pi v_{c0}^n\left(R_t^n \sin\pi\hat{d}^n - X_t^n \cos\pi\hat{d}^n\right). \tag{47}$$

C. Model Extensions

The derivation in the previous section is shown for the specific case of N DAB converters operating with single phase shift modulation. However, the model in [18] is capable of representing more general modulation schemes, including triple, dual, and extended phase shift modulation. Including these modulation schemes in the system-level model is a straightforward extension. The line current equations in (24)–(27) and block diagonal construction procedure in (33)–(36) apply regardless of modulation strategy. Only the submatrices $\frac{\partial f^n}{\partial x^n}$, $\frac{\partial f^n}{\partial \hat{d}^n}$, $\frac{\partial g^n}{\partial x^n}$, and $\frac{\partial g^n}{\partial \hat{d}^n}$ will change. These derivative submatrices are given for general modulation strategies in [18].

Similarly, while the focus of this study is the DAB topology, the model combination procedure applies equally for other converter topologies. For other topologies, the algebraic state variable $\hat{d}$ and correction equation $g(\cdot)$ are not necessary, and can simply be omitted. Only the derivative submatrix $\frac{\partial f^n}{\partial x^n}$ is required to complete the system-level model.

D. Model Limitations

The large-signal model provides accurate descriptions of converter and system dynamics. Since discontinuous switching functions are eliminated in the derivation, the models are computationally efficient and suitable for large-scale system simulations. However, eliminating switching functions presents some limitations in terms of model accuracy. Mathematically, the source of the model's limitations is the same as the source of classical average models' limitations: truncation of the Fourier series. For classical average models, only dc Fourier series terms are considered, and all higher terms are neglected. This is equivalent to assuming that switching ripple is small [30]. As a result, average models are unable to predict periodic oscillations, such as capacitor voltage ripple. More Fourier series terms are included in GAM, but to limit model complexity, typically only the dc and fundamental frequency terms are used to derive models.

Due to the decoupling effect discussed in Section II-C, the present models consist of states which are either purely dc average terms or first harmonic ac terms [21]. For dc average states, such as capacitor voltages, the model is subject to the same limitations of classical average models (i.e., ripple voltage is neglected). For the purposes of system-level simulation, this sacrifice is justified. Voltage ripple components are typically small for well-designed converters, and closed-loop control systems typically filter out switching-frequency feedback components to minimize their effect on dynamic performance. As a result, the effect of ripple voltage on system-level dynamics is minimal for systems of well-design converters. However, since the proposed models are not able to describe ripple voltage effects, they may provide incorrect predictions for converters, which are damaged or poorly designed. When prediction of ripple components is of critical importance, models that eliminate switching functions through averaging should not be used.

The GAM states which contain ac terms are similarly limited. In the present case, only transformer current states consist of purely ac terms. Since these terms are limited to fundamental frequency components, the model predictions consist of sinusoids at the switching frequency. However, it is possible to improve the accuracy of these predictions by reconstructing the truncated components of the transformer currents' Fourier

series. A new method for reconstructing these terms is described in the following section.

One additional model limitation is representation of switching dead time. The switching signal Fourier series are derived under the assumption of ideal switching behavior, i.e., zero dead time. However, dead time is a practical necessity to prevent shoot-through faults. Describing dead time requires a significant increase in model complexity, but is only necessary for a small fraction of the DAB converter's operating space. In particular, dead time effects become noticeable at very low load conditions [39]. However, these conditions are typically avoided due to the DAB's limited soft switching capabilities at light loading. When operating regions affected by dead time cannot be avoided, compensation schemes may be used to mitigate undesirable dead time effects [40]. Dead time is problematic for all DAB modeling approaches in the literature, either in the form of accuracy limitations or increased complexity. Further research is needed to identify computationally efficient methods for modeling dead time effects.

IV. Transformer Current Reconstruction

The preceding sections have described a general-purpose large-signal model. This section is concerned with improving the fidelity of the time-domain transformer current representations. The following analysis is applicable to any DAB converter in the system; superscript n is dropped for readability. Let v_c, v_o, i_t, and d be state trajectories resulting a time-domain simulation of the proposed model. The voltages and phase shift are dc average variables, so the state trajectories are give trivially by the states of the proposed model. The transformer current is calculated from states i_{tR} and i_{tI} according to (5). The result is a sinusoidal approximation of the transformer current. This approximation is suitable for efficient small-signal analyses, but for many other purposes, such as evaluating device current stresses or analyzing zero voltage switching (ZVS) conditions, more accurate current representations are required. As a direct consequence of the correction factor equations used in the proposed model, it is possible to obtain accurate representations by reconstructing the full Fourier series for the transformer currents.

Let $v_p = s_1 v_c$ and $v_s = s_2 v_o$ be the voltages across the primary and secondary of the high frequency transformer. To simplify equations, assume that v_c and v_o may be approximated as constant during a single switching period. This scenario would result from sampling the continuous-time state trajectories at multiples of the switching period with a zero-order hold. The transformer current is the solution to the forced differential equation

$$L_t \dot{i}_t = v_p - v_s - i_t R_t. \tag{48}$$

The voltages can be expanded as Fourier series

$$v_p(\tau) = \sum_{k=1}^{\infty} a_k^p \cos \omega k\tau + b_k^p \sin \omega k\tau \tag{49}$$

$$v_s(\tau) = \sum_{k=1}^{\infty} a_k^s \cos \omega k\tau + b_k^s \sin \omega k\tau. \tag{50}$$

The coefficients are known, and equal to the Fourier series coefficients of s_1 and s_2 scaled by v_c and v_o, respectively. For single phase shift modulation, the coefficients are as follows:

$$a_k^p = 0 \qquad b_k^p = \begin{cases} \frac{4v_c}{k\pi} & k \text{ odd} \\ 0 & k \text{ even} \end{cases}$$

$$a_k^s = \begin{cases} \frac{-4v_o \sin dk\pi}{k\pi} & k \text{ odd} \\ 0 & k \text{ even} \end{cases} \qquad b_k^s = \begin{cases} \frac{4v_o \cos dk\pi}{k\pi} & k \text{ odd} \\ 0 & k \text{ even.} \end{cases}$$

For any given k, the corresponding current solution may be determined using Laplace transforms

$$i_t(s)(L_t s + R_t) = \frac{(a_k^p - a_k^s)s}{s^2 + (\omega k)^2} + \frac{(b_k^p - b_k^s)\omega k}{s^2 + (\omega k)^2}. \tag{51}$$

Alternatively, this may be written as

$$i_t(s) = \left(\frac{1}{L_t s + R_t}\right)\left(\frac{a_k^v s + b_k^v \omega k}{s^2 + (\omega k)^2}\right) \tag{52}$$

where $a_k^v = a_k^p - a_k^s$ and $b_k^v = b_k^p - b_k^s$. The partial fraction decomposition of this equation is

$$i_t(s) = \frac{1}{L_t}\left(\frac{b_k^v \omega k - a_k^v(\frac{R_t}{L_t})}{(\omega k)^2 + (\frac{R_t}{L_t})^2}\right)\left(\frac{1}{s + (\frac{R_t}{L_t})} - \frac{s}{s^2 + (\omega k)^2}\right) + \frac{1}{\omega k L_t}\left[a_k^v + \frac{R_t}{L_t}\left(\frac{b_k^v \omega k - a_k^v(\frac{R_t}{L_t})}{(\omega k)^2 + (\frac{R_t}{L_t})^2}\right)\right]\left(\frac{\omega k}{s^2 + (\omega k)^2}\right). \tag{53}$$

Taking the inverse Laplace transform yields the time-domain current solution

$$i_t(\tau) = \frac{1}{L_t}\left(\frac{b_k^v \omega k - a_k^v(\frac{R_t}{L_t})}{(\omega k)^2 + (\frac{R_t}{L_t})^2}\right)\left(e^{\frac{-R_t}{L_t}\tau} - \cos \omega k\tau\right) + \frac{1}{\omega k L_t}\left[a_k^v + \frac{R_t}{L_t}\left(\frac{b_k^v \omega k - a_k^v(\frac{R_t}{L_t})}{(\omega k)^2 + (\frac{R_t}{L_t})^2}\right)\right]\sin \omega k\tau. \tag{54}$$

The quantity of interest is the periodic solution, so the decaying exponential term may be discarded. The full current solution is the summation

$$i_t(\tau) = \frac{1}{L_t}\sum_{k=1}^{\infty} a_k^i \cos \omega k\tau + b_k^i \sin \omega k\tau \tag{55}$$

where a_k^i and b_k^i are the Fourier series coefficients of the transformer current, given by the following:

$$a_k^i = -\left(\frac{b_k^v \omega k - a_k^v(\frac{R_t}{L_t})}{(\omega k)^2 + (\frac{R_t}{L_t})^2}\right) \tag{56}$$

$$b_k^i = \frac{1}{\omega k}\left(a_k^v + \frac{R_t}{L_t}\left(\frac{b_k^v \omega k - a_k^v(\frac{R_t}{L_t})}{(\omega k)^2 + (\frac{R_t}{L_t})^2}\right)\right). \tag{57}$$

Since this method is applied offline using state trajectories from the base model, the currents for each converter in a given system and each time range of interest may be calculated separately. Moreover, the zero-order-hold approximation allows each switching period to be treated independently. This means that every combination of converter, harmonic number,

and switching period in the time range of interest may be considered as an independent, parallel computation.

This harmonic reconstruction method provides a unified approach for predicting DAB transformer currents. The derivation applies regardless of modulation strategy. When applying this method to different modulation schemes, only the Fourier series coefficients a_k^p, b_k^p, a_k^s, and b_k^s change. In [18], the base model and correction factors are derived for triple phase shift modulation, since it is very general. Single, dual, and extended phase shift are special cases of triple phase shift modulation. Using the terminology from [18], the Fourier series coefficients for triple phase shift are as follows:

$$a_k^p = \begin{cases} \frac{2v_c \sin(d_p k\pi)}{k\pi}, & k \text{ odd} \\ 0, & k \text{ even} \end{cases}$$

$$b_k^p = \begin{cases} \frac{2v_c (1-\cos(d_p k\pi))}{k\pi}, & k \text{ odd} \\ 0, & k \text{ even} \end{cases}$$

$$a_k^s = \begin{cases} \frac{2v_o \sin(d_\phi k\pi) - 2v_o \sin((d_s+d_\phi)k\pi)}{k\pi}, & k \text{ odd} \\ 0, & k \text{ even} \end{cases}$$

$$b_k^s = \begin{cases} \frac{2v_o \cos(d_\phi k\pi) - 2v_o \cos((d_s+d_\phi)k\pi)}{k\pi}, & k \text{ odd} \\ 0, & k \text{ even} \end{cases}$$

where d_p is the width of the pulse applied to the primary side of the transformer, d_s is the width of the pulse applied to the secondary side, and d_ϕ is the phase shift between the pulses. Note that for single and dual phase shift modulation, $d = d_\phi$. For more detailed information on triple phase shift modulation, the interested reader is encouraged to consult references [18], [41].

V. Verification

Simulations and hardware experiments were used to validate the proposed methods. The objective of the simulation experiments is to show that, in both transient and steady-state conditions, the proposed model and harmonic reconstruction method provide accuracy equivalent to switching simulations with significantly reduced computation time. The objective of the hardware validation is to show the accuracy of the proposed methods with respect to real-world converters.

A. 7-Bus Simulation

One of the key applications of the proposed model is efficient and accurate time-domain simulation. To assess the model performance in this capacity, results of system-level simulations performed in PLECS are compared with results obtained through numerical integration of the model equations. Switching simulations are highly accurate but become computationally inefficient as the number of converters in the system increases due to the increased burden of zero-crossing detection.

The system shown in Fig. 2 is considered as a case study. The system is organized as follows. Converter 1 regulates a nominal voltage of 48 V at bus 1. Converter 2 serves bus 4, a subordinate distribution bus, and regulates a nominal voltage of 42 V.

TABLE I
Control and Hardware Parameters for 7-Bus System

Parameter	Value	Parameter	Value
C_{in}^1, C_{in}^2, C_{in}^3	200 μF	C_{in}^4, C_{in}^5	40 μF
C_o^1, C_o^2, C_o^3	200 μF	C_o^4, C_o^5	40 μF
f_s^1	40 kHz	k_p^1 / k_i^1	0.01 / 15
f_s^2	60 kHz	k_p^2 / k_i^2	0.01 / 10
f_s^3	75 kHz	k_p^3 / k_i^3	0.01 / 25
f_s^4	100 kHz	k_p^4 / k_i^4	0.001 / 25
f_s^5	90 kHz	k_p^5 / k_i^5	0.005 / 25

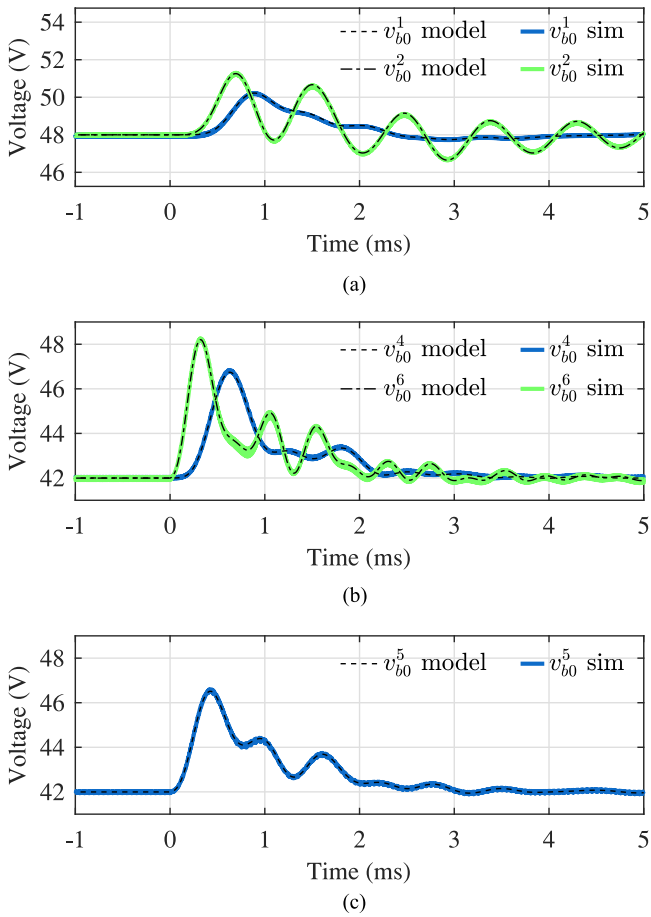

Fig. 3. Load disturbance responses of selected system bus voltages. Voltage v_{b0}^5 is shown separately since it is the only algebraic bus voltage state. (a) Bus voltages v_{b0}^1 and v_{b0}^2. (b) Bus voltages v_{b0}^4 and v_{b0}^6. (c) Bus voltage v_{b0}^5.

Converters 3, 4, and 5 serve bidirectional current source loads. The system may be understood as two subsystems, divided across converter 2. Buses 1, 2, and 3 comprise the 48 V subsystem; buses 4, 5, 6, and 7 comprise the 42 V subsystem. All lines have resistance $R_{ij} = 0.001\,\Omega$ and inductance $L_{ij} = 0.1$ mH. All high-frequency transformers have 1:1 turns ratios, winding resistance $R_t^n = 0.4\,\Omega$, and leakage inductance $L_t^n = 4\,\mu$H. Additional hardware and control parameters are given in Table I.

Comparisons of switching simulation and model results for a load disturbance transient are shown in Figs. 3 and 4.

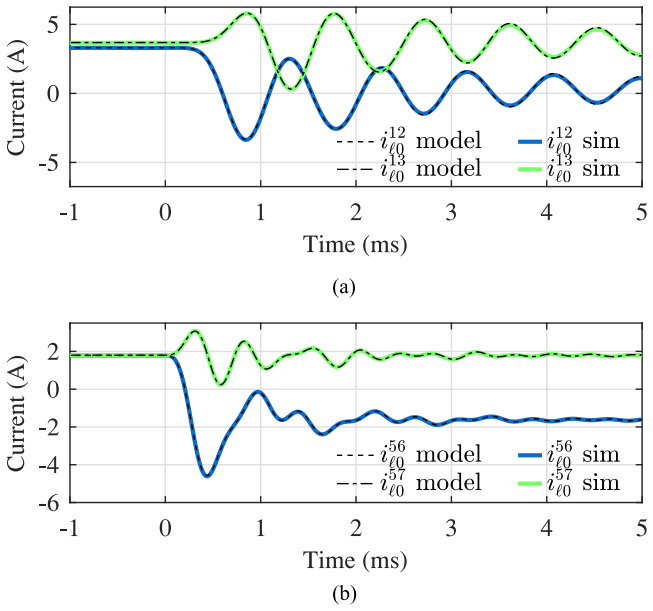

Fig. 4. Load disturbance responses of selected system line currents. (a) Line currents $i_{\ell 0}^{12}$ and $i_{\ell 0}^{13}$. (b) Line currents $i_{\ell 0}^{56}$ and $i_{\ell 0}^{57}$.

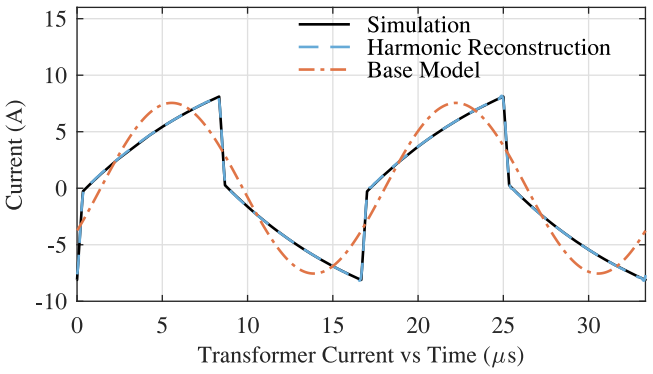

Fig. 5. Comparison of converter 2 transformer currents from simulation, results calculated using the proposed harmonic reconstruction method, and first harmonic approximations from the base model.

The disturbance consists of a step change in the load current of converter 4 at time $t = 0$ s, from $i_{L0}^4 = 2$ A to $i_{L0}^4 = -2$ A. The load currents for converters 3 and 5 remain fixed at $i_{L0}^3 = 4$ A and $i_{L0}^5 = 2$ A throughout. A selection of bus voltage responses are shown in Fig. 3; line current responses are shown in Fig. 4. The figures show that the model and switching simulation are consistent in both transient and steady-state response. The states not shown in these figures match with similar accuracy.

Despite the accuracy of the dc average states, the transformer currents predicted by the base model are only sinusoidal approximations of the actual transformer current. However, using the harmonic reconstruction method, the actual transformer currents may be calculated with high accuracy as well. A comparison of the transformer current for converter 2 from simulation, from the base model, and from the proposed harmonic reconstruction method is shown in Fig. 5. The reconstruction includes up to the 35th harmonic of the switching frequency. Since only

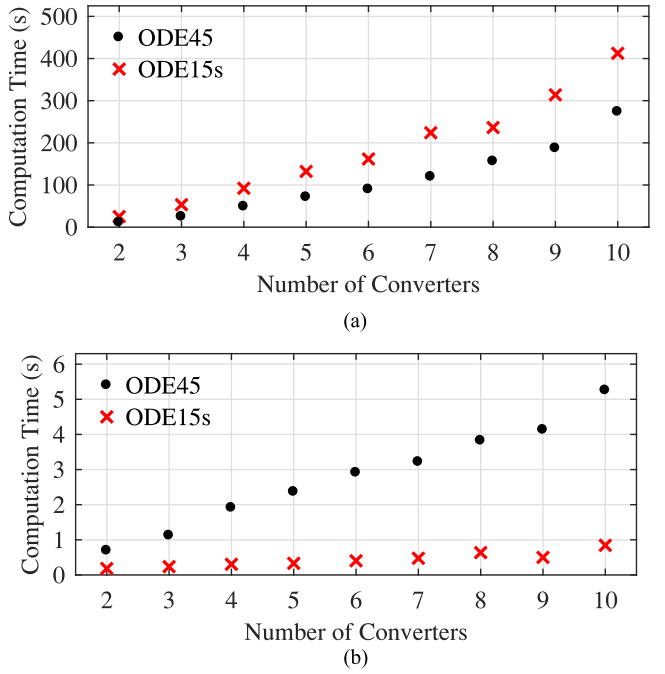

Fig. 6. Comparison of computation times for time-domain simulations using switching models (top) and proposed average models (bottom) by number of converters included in the system. (a) Switching model. (b) Average model.

odd harmonics are nonzero, this corresponds to 18 harmonic components.

B. Computation Time

The foremost advantage of using the model for time-domain simulation is execution time. In terms of computation time, the benefit of an average model over a switching model is fundamental. Eliminating the need for zero-crossing detection significantly reduces computational overhead. To illustrate this improvement, computation times for simulations of a variety of multiconverter systems were recorded. To ensure fair comparison, both the switching simulation and average model were implemented in Simulink. All simulations consider a time range of 50 ms with maximum time step size of 1 ms and error tolerance of 10^{-5}.

Results of the computation time comparisons are shown in Fig. 6. For consistency, standard explicit and implicit solvers were used for both systems. Since the average model is a DAE system, the numerical integration algorithm must solve both the dynamic and algebraic state equations. The implicit solver (ODE15s) simultaneously solves dynamic and algebraic equations, and is therefore the more appropriate solver for the proposed model. The explicit solver (ODE45) is less efficient for the average model, since the dynamic and algebraic equations separately at each time step. The switching model is a nonsparse ODE system, so it does not benefit from an implicit solver. Regardless of solver selection, simulation of the average model is significantly faster than simulation of the switching model. When appropriate solvers are used for both models, the computation times for the switching model are two orders of magnitude longer than those of the average model.

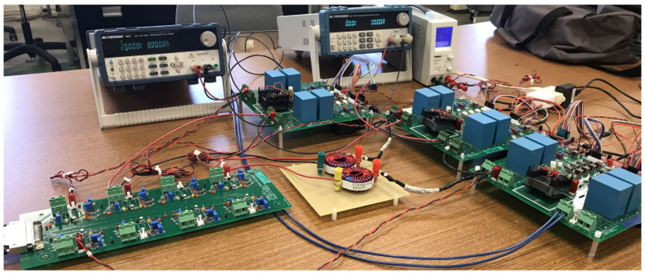

Fig. 7. Hardware testbed.

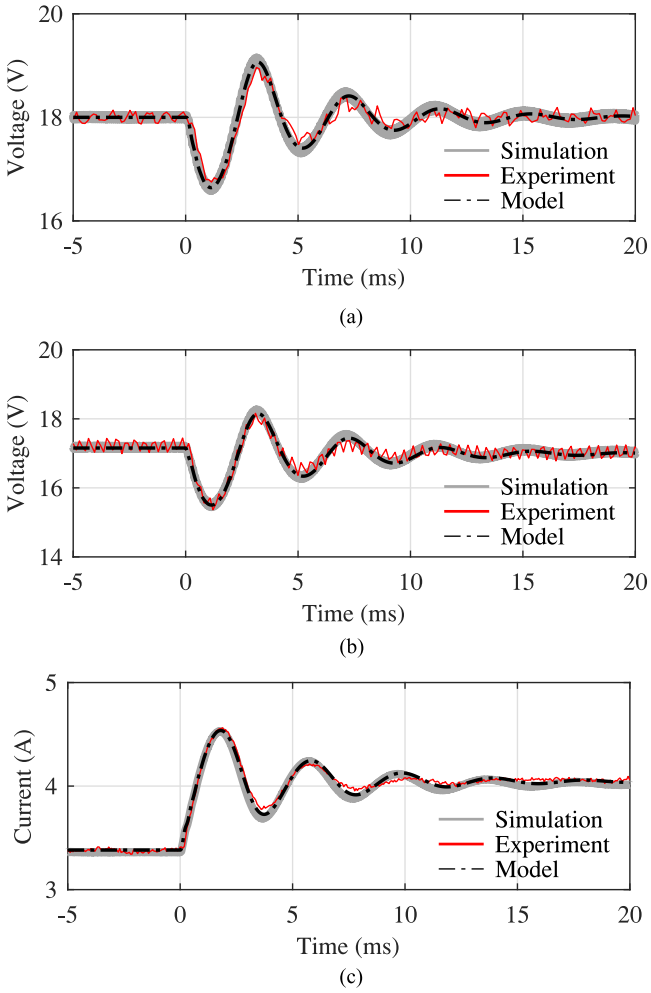

Fig. 8. Comparison of simulation, hardware measurements, and model predictions for bus voltage and line current states. (a) Converter 1 output voltage. (b) Converter 2 input voltage. (c) Line current.

C. Hardware Experiment

The hardware testbed is shown in Fig. 7. The testbed consists of two DAB converters connected in series: the output of converter 1 is connected to the input of converter 2 through a line impedance. The line impedance has both resistive (0.25 Ω) and inductive (100 μH) components. The output of converter 2 is connected to a current source load, which steps from 3 to 3.5 A during the experiment. Both converters regulate output voltages of 18 V, and operate with switching frequencies of 80and 74.074 kHz, respectively. Control systems run independently on two TMS320F28377S digital signal processors (DSPs). Voltages and currents are logged externally during the test; internal state variables are logged through directly through the DSPs.

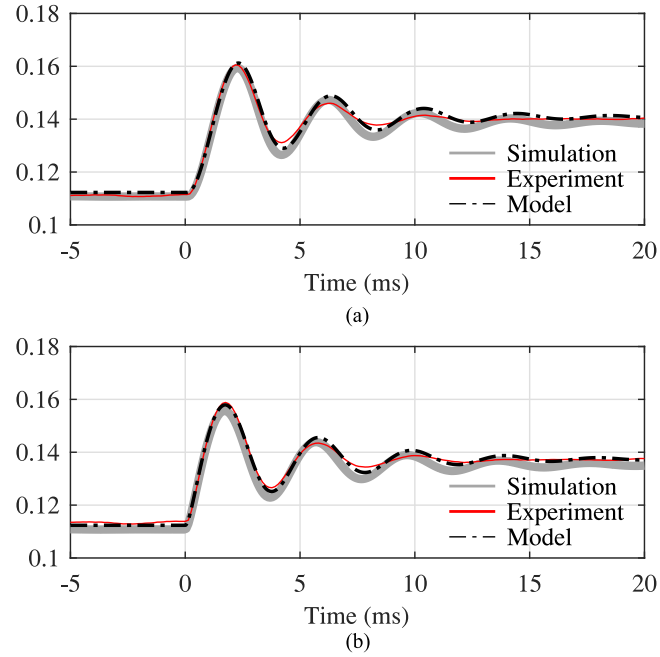

Fig. 9. Comparison of simulation, hardware measurements, and model predictions for controller integrator states. (a) Converter 1 integrator state. (b) Converter 2 integrator state.

TABLE II
STEADY STATE RESULTS FOR 2-CONVERTER SYSTEM

Before Load Step			
State	Simulation	Experiment	Model
v_{o0}^1	18.00 V	18.00 V	18.00 V
v_{c0}^2	17.17 V	17.24 V	17.15 V
$i_{\ell 0}^{12}$	3.360 A	3.381 A	3.382 A
γ_0^1	0.111	0.111	0.112
γ_0^2	0.111	0.113	0.112
After Load Step			
State	Simulation	Experiment	Model
v_{o0}^1	18.00 V	18.00 V	18.01 V
v_{c0}^2	17.01 V	17.00 V	17.01 V
$i_{\ell 0}^{12}$	4.020 A	4.046 A	4.036 A
γ_0^1	0.139	0.140	0.140
γ_0^2	0.136	0.138	0.137

Comparisons of large-signal model predictions, switching simulations, and experimental results are shown in Figs. 8 and 9. Bus voltage and line current states are shown in Fig. 8, internal integrator states are shown in Fig. 9. Table II shows the numerical steady-state values before and after the load change. The results indicate that the proposed method accurately describes both the transient and steady-state response of the system, despite the difference in switching frequencies between converters.

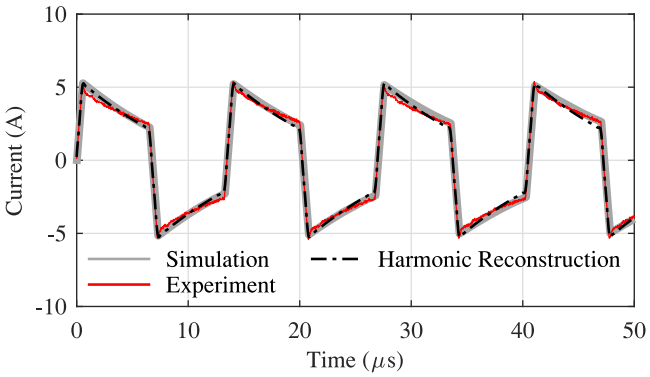

Fig. 10. Comparison of converter 2 transformer currents from simulation, hardware measurements, and harmonic reconstruction.

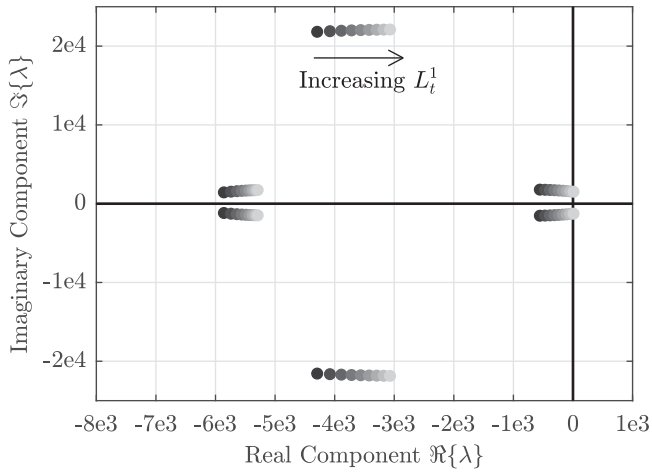

Fig. 11. Changes in eigenvalue loci for linearized 2-converter system as L_t^1 increases.

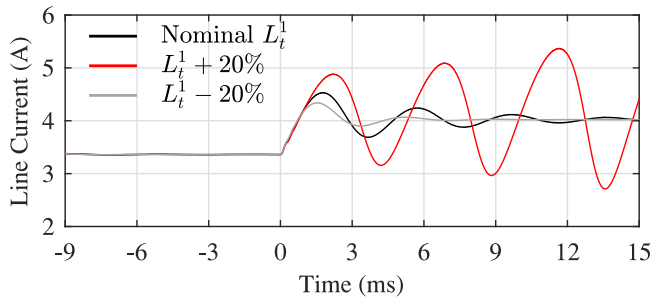

Fig. 12. Simulation results for 2-converter system with nominal L_t^1 and maximum/minimum L_t^1 within $\pm 20\%$ tolerance.

The significance of accurate integrator states is that they allow phase shift values to be determined accurately using (18). This is a distinct advantage over the earlier model in [21], which was affected by large-signal error.

To verify the functionality of the proposed harmonic reconstruction method, the transformer current of converter 2 is reconstructed and compared to measurements from the experiment. The comparison is shown in Fig. 10. These results demonstrate that the harmonic reconstruction approach accurately describes the real-world behavior of the transformer current.

D. Eigenvalue Analysis

The results in the previous sections specifically target applications of the proposed system-level model for time-domain simulation. Another important application is small-signal stability assessment. Eigenvalue analysis is a standard method of assessing stability, and is commonly used for ac microgrids and conventional power systems [23], [36]. The advantage of eigenvalue analysis is that the procedure applies in the same way regardless of the topology or power flow configuration; the disadvantage is that it requires a system-level dynamic model. However, the necessary large-signal models can easily be generated using the proposed model construction procedure. As an example, the stability of the 2-converter system is assessed via eigenvalue inspection. In particular, system stability is analyzed for changes in transformer leakage inductance within a prespecified range of hardware tolerance. While inductive elements are commonly modeled with constant parameters, their actual inductance may vary widely. The objective of this analysis is to determine the effect of variations in L_t^1 within a $\pm 20\%$ tolerance. This is accomplished by iterating through potential values of L_t^1 and observing changes in the locations of system eigenvalues.

In Fig. 11, eigenvalue loci are plotted on the complex plane for changes in L_t^1. The eigenvalues are plotted for L_t^1 ranging from -20% to $+20\%$ of the nominal inductance in 5% increments. Eigenvalue plots range from darker to lighter as L_t^1 increases. The 2-converter system has 10 total eigenvalues; only those relevant to system stability (those close to the imaginary axis) are shown in Fig. 11. The plot indicates that variations in L_t^1 produce significant changes in the eigenvalue loci. At the maximum value of L_t^1, the pair closest to the origin actually crosses the imaginary axis, indicating system instability. On the other hand, the lower values of L_t^1 are further into the left half plane, indicating faster and more damped transient responses. Simulations confirm the results of the eigenvalue analysis. Fig. 12 shows the current in the line connecting the two converters during the same load step shown in Fig. 8(c). Dynamic responses are shown for nominal L_t^1 and for values at the upper and lower extremes of the tolerance range. As expected, the higher value of inductance results in an unstable response, while the lower value produces a response with faster settling time and higher damping.

VI. Conclusion

Managing the tradeoff between accuracy and complexity is particularly difficult for multiconverter systems. Models must be simple enough to be used in large-scale system-level representations without sacrificing the accuracy necessary for converter-level analysis. This study presents two contributions that support this objective: a scalable model construction procedure and a method of predicting exact DAB transformer current waveforms.

The standard model generated by the proposed model construction procedure is compatible with the methods of

system-level analysis that are commonly applied in large-scale conventional power systems. Power systems techniques address problems of size and complexity by design; leveraging these methods extends the scope of applications for the proposed models. The construction process does not require the specification of a base period, despite the use of GAM to derive the base converter models. The system-level models are fully continuous in time, and provide efficient alternatives to switching simulations for time-domain analysis. Moreover, the models may be linearized for small-signal stability analyses that include the dynamic effects of the high-frequency transformer parameters. While DAB converters are the focus of this study, the system-level model construction procedure applies for any converter topology with accurate average models.

The scalability of this framework makes it effective for high-level analysis of large systems, but accuracy is also retained at the individual converter level. The harmonic reconstruction method increases the fidelity of high-frequency transformer current predictions without increasing the model complexity. The method calculates higher order harmonic components of the transformer current without including these components as states of the GAM. This reconstruction addresses one of the most important disadvantages of using GAM, and it ensures that the converter-level models provide sufficient detail to perform analyses relevant to switched-mode converter operation, such as predicting device stresses and ZVS conditions. Furthermore, since the method is applied offline, it does not contribute additional computational complexity when using the system-level model for time-domain simulations. Together, the methods presented here constitute a modeling framework that is suitable for both high-level and low-level analysis, and is accessible to both power electronics and power systems engineers.

REFERENCES

[1] R. W. A. A. DeDoncker, D. M. Divan, and M. H. Kheraluwala, "A three-phase soft-switched high-power-density dc/dc converter for high-power applications," *IEEE Trans. Ind. Appl.*, vol. 27, no. 1, pp. 63–73, Jan./Feb. 1991.

[2] M. N. Kheraluwala, R. W. Gascoigne, D. M. Divan, and E. D. Baumann, "Performance characterization of a high-power dual active bridge dc-to-dc converter," *IEEE Trans. Ind. Appl.*, vol. 28, no. 6, pp. 1294–1301, Nov./Dec. 1992.

[3] B. Zhao, Q. Song, W. Liu, and Y. Sun, "Overview of dual-active-bridge isolated bidirectional dc–dc converter for high-frequency-link power-conversion system," *IEEE Trans. Power Electron.*, vol. 29, no. 8, pp. 4091–4106, Aug. 2014.

[4] A. Q. Huang, "Medium-voltage solid-state transformer: Technology for a smarter and resilient grid," *IEEE Ind. Electron. Mag.*, vol. 10, no. 3, pp. 29–42, Sep. 2016.

[5] X. She, A. Q. Huang, and R. Burgos, "Review of solid-state transformer technologies and their application in power distribution systems," *IEEE J. Emerg. Sel. Topics Power Electron.*, vol. 1, no. 3, pp. 186–198, Sep. 2013.

[6] F. Krismer and J. W. Kolar, "Accurate small-signal model for the digital control of an automotive bidirectional dual active bridge," *IEEE Trans. Power Electron.*, vol. 24, no. 12, pp. 2756–2768, Dec. 2009.

[7] R. T. Naayagi, A. J. Forsyth, and R. Shuttleworth, "High-power bidirectional dc–dc converter for aerospace applications," *IEEE Trans. Power Electron.*, vol. 27, no. 11, pp. 4366–4379, Nov. 2012.

[8] B. Zahedi and L. E. Norum, "Modeling and simulation of all-electric ships with low-voltage dc hybrid power systems," *IEEE Trans. Power Electron.*, vol. 28, no. 10, pp. 4525–4537, Oct. 2013.

[9] I. Y. Chung *et al.*, "Integration of a bi-directional dc–dc converter model into a large-scale system simulation of a shipboard MVDC power system," in *Proc. IEEE Elect. Ship Technol. Symp.*, 2009, pp. 318–325.

[10] G. C. Verghese, M. E. Elbuluk, and J. G. Kassakian, "A general approach to sampled-data modeling for power electronic circuits," *IEEE Trans. Power Electron.*, vol. PE-1, no. 2, pp. 76–89, Apr. 1986.

[11] C. Zhao, S. D. Round, and J. W. Kolar, "Full-order averaging modelling of zero-voltage-switching phase-shift bidirectional dc–dc converters," *IET Power Electron.*, vol. 3, no. 3, pp. 400–410, 2010.

[12] L. Shi, W. Lei, Z. Li, J. Huang, Y. Cui, and Y. Wang, "Bilinear discrete-time modeling and stability analysis of the digitally controlled dual active bridge converter," *IEEE Trans. Power Electron.*, vol. 32, no. 11, pp. 8787–8799, Nov. 2017.

[13] H. Bai and C. Mi, "Eliminate reactive power and increase system efficiency of isolated bidirectional dual-active-bridge dc–dc converters using novel dual-phase-shift control," *IEEE Trans. Power Electron.*, vol. 23, no. 6, pp. 2905–2914, Nov. 2008.

[14] K. Zhang, Z. Shan, and J. Jatskevich, "Large- and small-signal average-value modeling of dual-active-bridge dc–dc converter considering power losses," *IEEE Trans. Power Electron.*, vol. 32, no. 3, pp. 1964–1974, Mar. 2017.

[15] F. Zhang, M. M. U. Rehman, R. Zane, and D. Maksimović, "Improved steady-state model of the dual-active-bridge converter," in *Proc. IEEE Energy Convers. Congr. Expo.*, 2015, pp. 630–636.

[16] S. R. Sanders, J. M. Noworolski, X. Z. Liu, and G. C. Verghese, "Generalized averaging method for power conversion circuits," *IEEE Trans. Power Electron.*, vol. 6, no. 2, pp. 251–259, Apr. 1991.

[17] H. Qin and J. W. Kimball, "Generalized average modeling of dual active bridge dc–dc converter," *IEEE Trans. Power Electron.*, vol. 27, no. 4, pp. 2078–2084, Apr. 2012.

[18] J. A. Mueller and J. Kimball, "An improved generalized average model of dc–dc dual active bridge converters," *IEEE Trans. Power Electron.*, vol. 33, no. 11, pp. 9975–9988, Nov. 2018.

[19] A. Emadi, "Modeling and analysis of multiconverter dc power electronic systems using the generalized state-space averaging method," *IEEE Trans. Ind. Electron.*, vol. 51, no. 3, pp. 661–668, Jun. 2004.

[20] A. Frances, R. Asensi, O. Garcia, R. Prieto, and J. Uceda, "Modeling electronic power converters in smart dc microgrids—An overview," *IEEE Trans. Smart Grid*, 2017.

[21] J. A. Mueller and J. W. Kimball, "Generalized average modeling of dc subsystem in solid state transformers," in *Proc. IEEE Energy Convers. Congr. Expo.*, Oct. 2017, pp. 1659–1666.

[22] M. L. Crow, "Numerical integration," in *Computational Methods for Electric Power Systems*, L. L. Grigsby. Ed. Boca Raton, FL, USA: CRC Press, 2016.

[23] P. W. Sauer and M. A. Pai, *Power System Dynamics and Stability*. Upper Saddle River, NJ, USA: Prentice Hall, 1998.

[24] R. J. Dirkman, "The simulation of general circuits containing ideal switches," in *Proc. IEEE Power Electron. Specialists Conf.*, 1987, pp. 185–194.

[25] A. M. Luciano and A. G. M. Strollo, "A fast time-domain algorithm for the simulation of switching power converters," *IEEE Trans. Power Electron.*, vol. 5, no. 3, pp. 363–370, Jul. 1990.

[26] D. Bedrosian and J. Vlach, "Time-domain analysis of networks with internally controlled switches," *IEEE Trans. Circuits Syst. I*, vol. 39, no. 3, pp. 199–212, Mar. 1992.

[27] N. Mohan, W. P. Robbins, T. M. Undeland, R. Nilssen, and O. Mo, "Simulation of power electronic and motion control systems–An overview," *Proc. IEEE*, vol. 82, no. 8, pp. 1287–1302, Aug. 1994.

[28] H. N. Chandra and V. J. Thottuvelil, "Modeling and analysis of computer power systems," in *Proc. 20th Annu. IEEE Power Electron. Specialists Conf.*, 1989, vol. 1, pp. 144–151.

[29] D. Maksimovic, A. M. Stankovic, V. J. Thottuvelil, and G. C. Verghese, "Modeling and simulation of power electronic converters," *Proc. IEEE*, vol. 89, no. 6, pp. 898–912, Jun. 2001.

[30] R. W. Erickson, S. Cuk, and R. D. Middlebrook, "Large-signal modelling and analysis of switching regulators," in *Proc. IEEE Power Electron. Specialists Conf.*, 1982, pp. 240–250.

[31] R. D. Middlebrook and S. Cuk, "A general unified approach to modelling switching-converter power stages," in *Proc. IEEE Power Electron. Specialists Conf.*, 1976, pp. 18–34.

[32] G. W. Wester and R. D. Middlebrook, "Low-frequency characterization of switched dc-dc converters," *IEEE Trans. Aerosp. Electron. Syst.*, vol. AES-9, no. 3, pp. 376–385, May 1973.

[33] B. H. Cho and F. C. Y. Lee, "Modeling and analysis of spacecraft power systems," *IEEE Trans. Power Electron.*, vol. 3, no. 1, pp. 44–54, Jan. 1988.
[34] P. T. Krein, J. Bentsman, R. M. Bass, and B. L. Lesieutre, "On the use of averaging for the analysis of power electronic systems," *IEEE Trans. Power Electron.*, vol. 5, no. 2, pp. 182–190, Apr. 1990.
[35] A. Riccobono and E. Santi, "Comprehensive review of stability criteria for dc power distribution systems," *IEEE Trans. Ind. Appl.*, vol. 50, no. 5, pp. 3525–3535, Sep./Oct. 2014.
[36] P. Kundur, N. J. Balu, and M. G. Lauby, *Power System Stability and Control* (EPRI Power System Engineering Series). New York, NY, USA: McGraw-Hill, 1994.
[37] S. Bacha, I. Munteanu, and A. I. Bratcu, *Power Electronic Converters Modeling and Control: With Case Studies* (Advanced Textbooks in Control and Signal Processing Series). London, U.K.: Springer, 2014.
[38] S. S. Shah and S. Bhattacharya, "Large & small signal modeling of dual active bridge converter using improved first harmonic approximation," in *Proc. IEEE Appl. Power Electron. Conf. Expo.*, 2017, pp. 1175–1182.
[39] B. Zhao, Q. Song, W. Liu, and Y. Sun, "Dead-time effect of the high-frequency isolated bidirectional full-bridge dc–dc converter: Comprehensive theoretical analysis and experimental verification," *IEEE Trans. Power Electron.*, vol. 29, no. 4, pp. 1667–1680, Apr. 2014.
[40] D. Segaran, D. G. Holmes, and B. P. McGrath, "Enhanced load step response for a bidirectional dc–dc converter," *IEEE Trans. Power Electron.*, vol. 28, no. 1, pp. 371–379, Jan. 2013.
[41] J. Huang, Y. Wang, Z. Li, and W. Lei, "Unified triple-phase-shift control to minimize current stress and achieve full soft-switching of isolated bidirectional dc-dc converter," *IEEE Trans. Ind. Electron.*, vol. 63, no. 7, pp. 4169–4179, Jul. 2016.

Jacob A. Mueller (M'18) received the B.S., M.S., and Ph.D. degrees in electrical engineering from Missouri University of Science and Technology, Rolla, Missouri, in 2012, 2014, and 2018, respectively.

He is a Postdoctoral Appointee with the Energy Storage Technology and Systems Department, Sandia National Laboratories, Albuquerque, NM, USA. His research interests include modeling and control of power electronics, optimization of energy storage systems, and nonintrusive load monitoring.

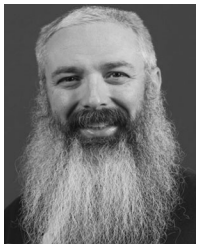

Jonathan W. Kimball (SM'05) received the B.S. degree in electrical and computer engineering from Carnegie Mellon University, Pittsburgh, PA, USA, in 1994, the M.S. degree in electrical engineering from the University of Illinois at Urbana-Champaign (Illinois), Champaign, IL, USA, in 1996, and the Ph.D. degree in electrical and computer engineering from Illinois, Champaign, IL, USA, in 2007.

From 1996 to 1998, he worked for Motorola, Phoenix, AZ, USA, designing IGBT modules for industrial applications. He then joined Baldor Electric, Fort Smith, AR, where he designed industrial adjustable speed drives ranging 1150 hp. In 2003, he returned to Illinois as a Research Engineer (later a Senior Research Engineer). Later in 2003, he co-founded SmartSpark Energy Systems, Inc., in Champaign, IL, USA, and served as a Vice President of Engineering. He joined the Faculty of Missouri S&T (formerly the University of Missouri-Rolla) in 2008 as an Assistant Professor. He was promoted to Associate Professor in 2014 and to Professor of Electrical and Computer Engineering in 2018. From 2016 to 2018, he was also a Dean's Scholar of the College of Engineering and Computing. His research interests include microgrids, switched-capacitor converters, and cyber-physical systems.

Dr. Kimball is a Member of Eta Kappa Nu, Tau Beta Pi, and Phi Kappa Phi. He is a Licensed Professional Engineer in the State of Illinois. He was the General Chair of the IEEE Applied Power Electronics Conference in 2017 and continues to serve on its steering committee.